Modeling of global variations and ring shadowing in Saturn's ionosphere

L.E. Moore [a], M. Mendillo [a,*], I.C.F. Müller-Wodarg [a,b], D.L. Murr [c]

[a] *Center for Space Physics, Boston University, 725 Commonwealth Avenue, Boston, MA 02215, USA*
[b] *Space and Atmospheric Physics Group, Imperial College London, London, UK*
[c] *Thayer School of Engineering, Dartmouth College, Hanover, NH, USA*

Abstract

A time-dependent one-dimensional model of Saturn's ionosphere has been developed as an intermediate step towards a fully coupled Saturn Thermosphere–Ionosphere Model (STIM). A global circulation model (GCM) of the thermosphere provides the latitude and local time dependent neutral atmosphere, from which a globally varying ionosphere is calculated. Four ion species are used (H^+, H_2^+, H_3^+, and He^+) with current cross-sections and reaction rates, and the SOLAR2000 model for the Sun's irradiance. Occultation data from the Voyager photopolarimeter system (PPS) are adapted to model the radial profile of the ultraviolet (UV) optical depth of the rings. Diurnal electron density peak values and heights are generated for all latitudes and two seasons under solar minimum and solar maximum conditions, both with and without shadowing from the rings. Saturn's lower ionosphere is shown to be in photochemical equilibrium, whereas diffusive processes are important in the topside. In agreement with previous 1-D models, the ionosphere is dominated by H^+ and H_3^+, with a peak electron density of $\sim 10^4$ electrons cm^{-3}. At low- and mid-latitudes, H^+ is the dominant ion, and the electron density exhibits a diurnal maximum during the mid-afternoon. At higher latitudes and shadowed latitudes (smaller ionizing fluxes), the diurnal maximum retreats towards noon, and the ratio of $[H^+]/[H_3^+]$ decreases, with H_3^+ becoming the dominant ion at altitudes near the peak (~ 1200–1600 km) for noon-time hours. Shadowing from the rings leads to attenuation of solar flux, the magnitude and latitudinal structure of which is seasonal. During solstice, the season for the Cassini spacecraft's encounter with Saturn, attenuation has a maximum of two orders of magnitude, causing a reduction in modeled peak electron densities and total electron column contents by as much as a factor of three. Calculations are performed that explore the parameter space for charge-exchange reactions of H^+ with vibrationally excited H_2, and for different influxes of H_2O, resulting in a maximum diurnal variation in electron density much weaker than the diurnal variations inferred from Voyager's Saturn Electrostatic Discharge (SED) measurements. Peak values of height-integrated Pedersen conductivities at high latitudes during solar maximum are modeled to be ~ 42 mho in the summer hemisphere during solstice and ~ 18 mho during equinox, indicating that even without ionization produced by auroral processes, magnetosphere–ionosphere coupling can be highly variable.
© 2004 Elsevier Inc. All rights reserved.

Keywords: Ionospheres; Planetary rings; Saturn; Saturn, atmosphere

1. Introduction

Little is known about the structure and behavior of Saturn's ionosphere. The existing measurements are five radio occultations from Pioneer 11 and Voyager 1 and 2 during 1979–1981 (see Atreya et al., 1984). These dawn/dusk occultations of Saturn's atmosphere revealed peak electron densities N_{max} of 0.6–2×10^4 cm^{-3} across latitudes spanning 36° to 73° N. The altitudes of the peak density h_{max} presented a more complex parameter to determine: there were high-altitude h_{max} values ranging from ~ 1900–2900 km in the observations, and secondary lower altitude peaks with electron densities n_e occasionally very close in magnitude to the high altitude peaks. As will be discussed later, this high level of observational variability in h_{max} for Saturn has introduced a profound level of theoretical uncertainty about the set of physical processes that govern Saturn's ionosphere.

* Corresponding author. Fax: 617-353-6463.
E-mail address: mendillo@bu.edu (M. Mendillo).

Models predating the observations (McElroy, 1973; Atreya and Donahue, 1975; Capone et al., 1977) predicted electron densities larger by an order of magnitude, and underpredicted the altitude of the peak electron density. In an attempt to reconcile simulated electron densities with the radio measurements, modelers (such as Waite, 1981) invoked two different methods to enhance the chemical recombination in Saturn's ionosphere by converting long-lived atomic ions into molecular ions that recombine quickly. Inclusion of the charge-exchange reaction between H^+ and vibrationally excited H_2 ($v \geqslant 4$) provides a simple atomic-to-molecular ion conversion mechanism that becomes the dominant loss of H^+ (e.g., McElroy, 1973; McConnell et al., 1982; Majeed and McConnell, 1991). Alternatively, an influx of H_2O or OH from Saturn's rings results in slightly more complicated recombination chemistry, the net result being depletion of H^+ relative to molecular ions (e.g., Shimizu, 1980; Connerney and Waite, 1984; Waite and Cravens, 1987; Majeed and McConnell, 1991). There is no reason to exclude either loss process, although recent developments (Feuchtgruber et al., 1997; Moses et al., 2000) find an H_2O flux smaller than the flux considered by previous models, limiting the importance of chemical effects due to water in Saturn's ionosphere and relegating H_2O influx to a secondary loss process for H^+. Finally, there remain the possibilities of vertical transport of the plasma by either neutral winds or electric fields, or diurnal changes in $n_e(h)$ profiles associated with upward/downward plasmaspheric fluxes (e.g., McConnell et al., 1982; Majeed and McConnell, 1991, 1996; Moses and Bass, 2000).

Diurnal ionospheric behavior is even more poorly constrained, and more controversial: the fly-by radio occultation results pertain only to dawn and dusk local times, where N_{max} values can differ by a factor of ~ 3, yet diurnal electron density variations of two orders of magnitude were derived from Voyager radio experiments that measured electrostatic discharges in Saturn's atmosphere (Kaiser et al., 1984). No model to date has been able to reproduce such a diurnal variation in N_{max}. Modeled variations are less than a factor of 5, which has caused some expressions of uncertainty about the assumptions used in the interpretation of the Saturn electrostatic discharge (SED) measurements (Majeed and McConnell, 1996). Further observations would help to sort out whether the N_{max} variations inferred from SEDs are typical of diurnal behavior at Saturn, or whether they represent an unusual atmospheric situation.

The current status of ionospheric science at Saturn is thus one where advances in theoretical considerations and modeling are stunted by the sparse (and often controversial) datasets that would otherwise be used to validate and/or constrain models. The early, pioneering models mentioned above explored physical parameter space within the context of a few vertical profiles and a single diurnal pattern obtained by satellite fly-by diagnostics. The same parameter space is extended here to a global context, both to investigate overall morphology patterns predicted by existing accepted mecha-

nisms, and to help define the observational realm for upcoming measurements, in particular, the rich data set Cassini will hopefully provide.

Photochemistry and plasma diffusion are the two dominant processes in Saturn's ionosphere. Alterations may then arise from plasma transport driven by neutral winds, electrodynamics, secondary ionization, and charged particle precipitation, in addition to other more Saturn-specific possibilities, such as shadowing by the rings. An ideal model of Saturn's atmosphere would include all of these effects in three dimensions. This is the goal of the Saturn Thermosphere–Ionosphere Model (STIM), being prepared in time for the arrival of the Cassini spacecraft at Saturn in 2004. STIM's thermospheric portion is a global circulation model (GCM) that derives global distributions of neutral atmospheric characteristics—such as composition, temperatures and winds (Müller-Wodarg et al., 2004). The ionospheric model is currently a one-dimensional time-dependent model that is coupled computationally to the thermospheric results obtained independently in the GCM. Thus, while not a fully coupled model at this stage, the ionospheric processes of photochemistry and plasma diffusion act upon a changing neutral atmosphere. The ionospheric module also includes shadowing by the rings as a photochemical effect. This paper highlights the global morphology of a three-dimensional ionosphere, using the processes of photochemistry, plasma diffusion, and shadowing of sunlight by Saturn's rings.

2. Model

2.1. Overview

Any ionospheric model requires valid inputs of solar flux, background neutral atmosphere, chemical reaction rates, and cross-sections. Values for solar irradiance come from the empirical model, SOLAR2000 v1.23, and span 10–1000 Å (Tobiska et al., 2000, see Note added in proof). The 28-day solar periodicity was removed from the solar fluxes by taking two-week averages of a solar maximum period (14–27 September 1996, $\langle F10.7 \rangle \sim 70$) and a solar minimum period (1–14 January 1990, $\langle F10.7 \rangle \sim 180$).

Photoionization and photoabsorption cross-sections (Appendix A) are taken from Yan et al. (1998) for He; Samson (1966) for H; and a combination of Backx et al. (1976), Dujardin et al. (1987), Chung et al. (1993), and Yan et al. (1998) for H_2. The chemistry and reaction rates for the ionospheric module are given in Table 1.

Global structure of the neutral atmosphere is determined within the thermospheric GCM of STIM, using identical solar fluxes and cross-sections. The GCM solves self-consistently the three-dimensional time-dependent Navier–Stokes equations of energy, momentum and continuity by explicit time integration. The resolution for this study is $6°$ in latitude, $10°$ in longitude, and 2–5 sec in time. GCM cal-

Table 1
Photoionization, charge exchange, and electron–ion recombination rates

	Reaction	[a]Rate constant	[c]Reference
Photoionization:			
j_1	$H + h\nu \rightarrow H^+ + e^-$	1.2×10^{-9}	[d]Model
j_2	$H_2 + h\nu \rightarrow H_2^+ + e^-$	5.6×10^{-10}	[d]Model
j_3	$\rightarrow H^+ + H + e^-$	6.3×10^{-12}	[d]Model
j_4	$\rightarrow 2H^+ + 2e^-$	5.4×10^{-13}	[d]Model
j_5	$He + h\nu \rightarrow He^+ + e^-$	3.5×10^{-9}	[d]Model
Charge exchange:			
k_1	$H^+ + H_2 (v \geqslant 4) \rightarrow H_2^+ + H$	See text (Eq. (7))	–
k_2	$H^+ + H_2 + M \rightarrow H_3^+ + M$	[b]3.2×10^{-29}	2
k_3	$H_2^+ + H_2 \rightarrow H_3^+ + H$	2.0×10^{-9}	2
k_4	$H_2^+ + H \rightarrow H^+ + H_2$	6.4×10^{-10}	3
k_5	$He^+ + H_2 \rightarrow H^+ + H + He$	$1.0 \times 10^{-9}e^{-5700/T}$	1
k_6	$\rightarrow H_2^+ + He$	9.35×10^{-15}	3
k_7	$H^+ + CH_4 \rightarrow$ components	4.5×10^{-9}	2
k_8	$H_2^+ + CH_4 \rightarrow$ components	3.53×10^{-9}	2
k_9	$H_3^+ + CH_4 \rightarrow$ components	2.4×10^{-9}	3
k_{10}	$He^+ + CH_4 \rightarrow$ components	1.7×10^{-9}	2
k_{11}	$H^+ + H_2O \rightarrow H_2O^+ + H$	8.2×10^{-9}	3
k_{12}	$H_2^+ + H_2O \rightarrow H_2O^+ + H_2$	3.87×10^{-9}	3
k_{13}	$\rightarrow H_3O^+ + H$	3.43×10^{-9}	3
k_{14}	$H_3^+ + H_2O \rightarrow H_3O^+ + H_2$	5.3×10^{-9}	3
Recombination:			
α_1	$H^+ + e^- \rightarrow H$	$1.91 \times 10^{-10}T^{-0.7}$	2
α_2	$He^+ + e^- \rightarrow He$	$1.91 \times 10^{-10}T^{-0.7}$	2
α_3	$H_2^+ + e^- \rightarrow H$	$2.25 \times 10^{-6}T^{-0.4}$	2
α_4	$H_3^+ + e^- \rightarrow H_2 + H$	$7.62 \times 10^{-7}T^{-0.5}$	2
α_5	$\rightarrow 3H$	$9.7 \times 10^{-7}T^{-0.5}$	2
α_6	$H_2O^+ + e^- \rightarrow OH + H$	$2.77 \times 10^{-6}T^{-0.5}$	4
α_7	$\rightarrow O + H_2$	$3.46 \times 10^{-6}T^{-0.5}$	4
α_8	$H_3O^+ + e^- \rightarrow H_2O + H$	$6.06 \times 10^{-6}T^{-0.5}$	4
α_9	$\rightarrow OH + 2H$	$1.13 \times 10^{-5}T^{-0.5}$	4

[a] sec^{-1} for j_i, $cm^3\ sec^{-1}$ for k_i and α_i.
[b] $cm^6\ sec^{-1}$.
[c] 1: Moses and Bass (2000), 2: Kim and Fox (1994), 3: Anicich (1993), 4: Millar et al. (1997).
[d] Computed at peak during solar maximum for overhead illumination.

culations are performed on a pressure grid spanning 10^{-4} to 10^{-10} mbar (~ 800–4000 km) with 0.25 scale height steps. Pressure levels are converted to height assuming a spherical atmosphere (Müller-Wodarg et al., 2004). Perturbations arising from Saturn's oblateness and rotation will be addressed in a future study.

Saturn's observed exospheric neutral temperatures are not produced with solar EUV heating alone, a fact that holds true for the other giant planets as well (Gladstone et al., 2002; Yelle and Miller, 2004). In order to model the observed temperatures, additional sources of heating are necessary. The atmosphere in this study employs a representation of wave heating from below as well as solar heating from above (Müller-Wodarg et al., 2004). Typical thermospheric variations produced by a zenith angle dependent solar source and constant wave-heating sources are plotted in Fig. 1a, which shows neutral profiles for the sub-solar point during southern summer for solar maximum and solar minimum.

Typical variations in latitude are given in Figs. 1b and 1c. Variations in local time are much smaller, and therefore not plotted.

The 1-D ionospheric model solves the one-dimensional ion continuity equations,

$$\frac{\partial n_i^+}{\partial t} = P_i - L_i - \frac{\partial \phi_i}{\partial z}. \qquad (1)$$

Ion production ($P_i = A_i n_i$) can come from photoionization ($A_i = j_i$) or charge-exchange reactions ($A_i = k_{ij}n_j^+$). Loss ($L_i = B_i n_i^+$) is either recombination ($B_i = \alpha_i n_e$) or charge-exchange ($B_i = k_{ij}n_j$). Under this notation A_i and B_i are generic production and loss rates (sec^{-1}) for the species n_i^+; j_i is the photoionization rate (sec^{-1}) of n_i; k_{ij} is the rate coefficient for a charge-exchange reaction between n_i and n_j ($cm^3\ sec^{-1}$); and α_i is the recombination coefficient for n_i^+ ($cm^3\ sec^{-1}$). Electron density is taken to be the sum of the individual ion densities.
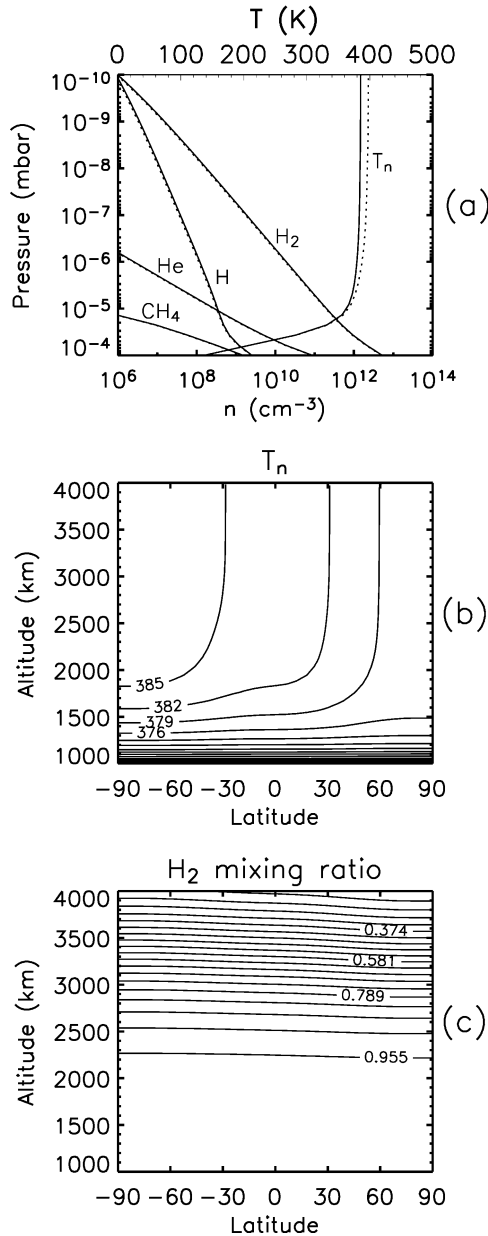
Neutral Atmosphere

Fig. 1. (a) Diurnally averaged GCM determined neutral atmosphere for 30° N latitude during southern summer. Solid lines represent solar minimum and dotted lines represent solar maximum. (b) Diurnally averaged neutral temperature contours for solar maximum southern summer. (c) Diurnally averaged H_2 mixing ratios for solar maximum southern summer. Neutral atmospheric variations in local time are much smaller than the latitudinal and solar cycle variations displayed here.

The ion drift velocity v_i (where plasma flux $\phi_i = n_i^+ v_i$) of the major ion in the absence of neutral winds or electrodynamical ($\mathbf{E} \times \mathbf{B}$) drifts is

$$v_i = -D_a \sin^2 I \left(\frac{1}{n_i^+} \frac{\partial n_i^+}{\partial z} + \frac{1}{H_p} + \frac{1}{T_p} \frac{\partial T_p}{\partial z} \right), \quad (2)$$

where D_a is the ambipolar diffusion coefficient, I is the magnetic dip angle, T_p is the plasma temperature (= $[T_e +$

$T_i]/2$). The plasma scale height H_p is given by

$$H_p = \frac{kT_p}{(\frac{m_i}{2})g}, \quad (3)$$

where k is Boltzmann's constant, m_i is the ion mass, and g the acceleration of gravity at altitude z (Schunk and Nagy, 2000). Minor ions must diffuse through neutrals and other ions, interacting with the charge separation electric fields set up by the major ions. The resulting expression for minor ion drift velocity is

$$v_j = v_i - D_j \sin^2 I \left(\frac{1}{n_j^+} \frac{\partial n_j^+}{\partial z} + \frac{1}{H_j} + \frac{T_e}{T_j} \frac{1}{n_e} \frac{\partial n_e}{\partial z} \right.$$
$$\left. + \frac{1}{T_j} \frac{\partial (T_e + T_j)}{\partial z} \right). \quad (4)$$

Here the subscript j refers to a minor species, the subscript i refers to the major species, $H_j = kT_j/m_jg$, $D_j = kT_j/m_jv_{ji}$, and v_{ji} is the ion–neutral collision frequency (Schunk and Nagy, 2000). The assumptions that the variation of gravity with altitude is negligible ($\Delta z \sim \frac{1}{20}R_S$) and that stress effects are unimportant have been made in this formulation. The model does not yet self-consistently calculate temperatures, in which case $T_n = T_e = T_i = T_j$; terms involving temperature gradients are therefore not used, as the thermosphere is isothermal in the diffusive domain.

A solution to Eq. (1), where changes in electron density are small, is

$$\Delta n_i^+ = \left(\frac{P_i}{B_i} - n_{i\,o}^+ \right)\left(1 - e^{-B_i \Delta t} \right) - n_{i\,o}^+ v_i \frac{\Delta t}{\Delta z} + \Delta n_{i\,\text{in}}^+. \quad (5)$$

Such a solution is more accurate than a basic numerical approach (e.g., $\Delta n_i^+ = [P_i - L_i]\Delta t$), because it demonstrates an asymptotic approach to equilibrium in each time step, allowing larger and more accurate time steps without computational instability. The middle term is a loss for n_i^+ at altitude z, and it becomes a source for either z_{+1} or z_{-1}, depending on the sign of the drift. Thus, $\Delta n_{i\,\text{in}}^+$ represents the influx of ions from above and/or below.

Ion densities are calculated on an altitude grid spanning ~ 800–3400 km (pressures of 10^{-4}–10^{-10} mbar), where 0 km corresponds to the 1 bar pressure level. Grid spacing in altitude is variable; to match the GCM output, 33 grid points were used with grid point spacing $\sim 1/4$ the neutral scale height. The one-dimensional model is iterated in time until steady-state equilibrium is reached, where steady-state equilibrium is defined as having a day-to-day variability in electron density of less than 1%. Under this definition, equilibrium for the entire electron density profile is reached in 10–25 Saturn days (10.656 hr per Saturn day), depending on the geometry and inputs of the run. Equilibrium at the ionospheric peak is reached in a shorter period, ~ 2–5 Saturn days. For latitude resolution, 6° is used for global calculations, with resolution increased to 1° for ring-shadowed latitudes. Finally, time resolution varies throughout the day, depending on how fast the electron density is changing, but is typically around 60 sec.

2.2. Chemistry

Chemistry in Saturn's atmosphere becomes rather complicated below the homopause—thought to be located near 1000 km—where hydrocarbons and other complex molecules are more prevalent (see Moses and Bass, 2000, for a complete treatment of this issue). As the vast majority of Saturn's ionosphere results from the ionization and chemistry of molecular and atomic hydrogen, the STIM ionospheric module saves computational time by not including the hydrocarbon chemistry. Rather, CH_4 is the only complex molecule included in the model, and its role is simply to provide a chemical sink at the bottom side of the ionosphere for the various hydrogen/helium ions through reactions k_7–k_{10} in Table 1. As hydrocarbon ions are not tracked, the net result of converting hydrogen/helium ions to hydrocarbon ions is the loss of electron–ion pairs within each time step. Thus we do not portray ionospheric densities below 1000 km. Moses and Bass (2000) consider the hydrocarbon chemistry and find that it adds a shoulder of $\sim 10^3$ cm^{-3} to the electron density profile near ~ 800 km (10^{-4} mbar).

As first suggested by McElroy (1973), the charge exchange reaction between H^+ and vibrationally excited H_2 would become exothermic for vibrational levels $\nu = 4$ or greater. An additional loss reaction for H^+ in Saturn's ionosphere, reaction k_1, is therefore

$$H^+ + H_2(\nu \geqslant 4) \rightarrow H_2^+ + H. \qquad (6)$$

Unfortunately, the rate constant for this reaction is poorly constrained; it has not been measured in the laboratory, and it is difficult to determine the populations of vibrationally excited H_2 at Saturn. The rate constant for reaction k_1 has been estimated to be of order 2×10^{-9} cm^3 sec^{-1}— its maximum kinetic rate (e.g., Cravens, 1987; McConnell et al., 1982)—however ionospheric models attempting to fit the Voyager and Pioneer radio occultation data at Jupiter and Saturn have estimated the fraction of H_2 in the $\nu = 4$ or greater state to be 10^{-2}–10^{-6} (McConnell et al., 1982; Majeed et al., 1991; Majeed and McConnell, 1991, 1996). Thus, effective k_1 reaction rates in the literature range from $\sim 10^{-11}$–10^{-15} cm^3 sec^{-1} (where the *effective* rate uses the total H_2 density rather than the H_2 ($\nu \geqslant 4$) density).

Yelle (1988) showed that fluorescence scattering of solar radiation should be an important source of vibrational excitation at Jupiter and Saturn. Majeed et al. (1990, 1991) considered the effect of fluorescence on the distribution of the vibrational levels of H_2, and found that it was in fact the dominant source for $\nu \geqslant 3$. Moses and Bass (2000) applied the Majeed et al. calculations to their model of Saturn's ionosphere by assuming a gas kinetic rate modified by the H_2 ($\nu \geqslant 4$)/H_2 ratio

$$k_1 = 2 \times 10^{-9} \sum_{\nu=4}^{8} \exp\left[-\frac{(E_\nu - E_o)}{kT_\nu}\right] \text{cm}^3 \text{sec}^{-1}, \qquad (7)$$

where the vibrational temperatures are taken from Fig. 9b of Majeed et al. (1991). The STIM ionospheric module employs the same parameterization (Eq. (7)) of H_2 vibrational distributions for reaction k_1. This method is analogous to contemporary coefficients adopted at Jupiter, where the rate coefficient is parameterized as $k_1 = 1.0 \times 10^{-9} F(T_\nu)$ cm^3 sec^{-1}, and $F(T_\nu) = \exp(-\Delta E_{\nu=4}/kT_\nu)$, and $T_\nu = [1 + 0.7 \exp(4 \times 10^{-4} z - 0.4)]T$ (Maurellis, 1998; Maurellis and Cravens, 2001). However, either parameterization still provides a source of uncertainty in predicted ionospheric densities, as n_e is very sensitive to this reaction.

2.3. Ring shadowing

Voyager 2 measurements of the δ Sco occultation in 1981 revealed considerable absorption by Saturn's rings in the radio and the ultraviolet wavelength regimes (Sandel et al., 1982; Holberg et al., 1982; Esposito et al., 1983; Marouf et al., 1986). A coordinated ground-based study of the 28 Sgr occultation in 1989 expanded ring absorption data into the infrared (Nicholson et al., 2000). Comparisons between the δ Sco and 28 Sgr data sets revealed remarkable agreement in optical depth across all wavelengths, indicating that the majority of absorption in Saturn's rings is from solid body scattering, and that the ring optical depth profile has been relatively constant during the nine year interim (Nicholson et al., 2000). This description fits well with the particle distributions in the rings, which range from ~ 1 cm to 20 m, considerably larger than important ionizing wavelengths in Saturn's ionosphere (Marouf et al., 1983; French and Nicholson, 2000).

In addition to solid body scattering, absorption by a ring atmosphere (or other saturnian system gases) must be considered. Broadfoot et al. (1981) found an H atmosphere with a number density of ~ 600 cm^{-3}, and a column density of $\sim 10^{13}$ cm^{-2}, but no other constituents with UV signatures. The results of Broadfoot et al. are consistent with previous measurements of the H ring atmosphere (Weiser et al., 1977). Doyle et al. (1996) find a comparable cloud of OH, with $n \sim 700$ cm^{-3} and $N_{OH} \sim 10^{13}$ cm^{-2}. Measurements of the Titan hydrogen torus show that it is less dense by over an order of magnitude (Broadfoot et al., 1981). Such column densities do not significantly attenuate sunlight; the optical depth of a 900 Å photon in a hydrogen gas with density 600 cm^{-3} is $\sim 2.6 \times 10^9$ km ($\sim 4 \times 10^4$ Saturn radii).

To evaluate the effects of ring shadowing on the ionosphere, a model of UV optical depth as a function of ring radius was adopted from the Esposito et al. (1983) Voyager 2 photopolarimeter system (PPS) results. Figure 2 shows the adopted optical depth model in thick solid lines; the thin lines come from Infra-Red Telescope Facility (IRTF) measurements of the 28 Sgr occultation, which are available via the Planetary Data System's Rings Node (http://ringside.arc.nasa.gov). Note the remarkable agreement between the two profiles, despite the measurements
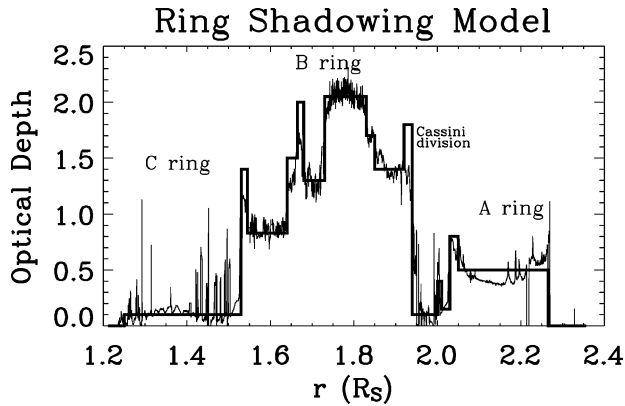
Ring Shadowing Model

Fig. 2. Comparison of the ultraviolet optical depth of the rings for normal incidence as measured by Voyager PPS stellar occultation (thick line; Esposito et al., 1983), and the infrared optical depth determined from IRTF stellar occultation measurements (thin line; Nicholson et al., 2000). The thick solid line is used for ring shadowing model calculations.

being made in different wavelength regimes and at different times. The only large deviation occurs around $1.9 R_S$ and has no noticeable effect on the ring-shadowed model calculations.

Solar flux passing through the rings is attenuated as

$$I(\delta, \phi) = I_o(\delta, \phi) \exp\left[-\frac{\tau(\delta, \phi)}{\sin \delta}\right], \qquad (8)$$

where δ is the solar declination, ϕ geographic latitude, and τ optical depth normal to the ring plane. Brinkman and McGregor (1979) were the first to calculate the effect of the rings on solar insolation, however questions were raised over terms in the formulation (Waite, 1981), and so an independent derivation has been performed here.

As Voyager PPS absorption data are for 2640 Å, it is assumed that the measured optical depths hold for all ionizing wavelengths (i.e., 10–912 Å). Some confidence is gained in this extrapolation from the apparent lack of wavelength dependence in the available measurements of optical depth (all > 912 Å) and from the relatively minor absorption of photons by rarefied gases in Saturn's rings and torus. Calculations with modified versions of the optical depth profile in Fig. 2 reveal slightly different results, but are qualitatively the same.

2.4. Photochemical equilibrium and plasma diffusion regimes

Though the model includes diffusion, it is useful to demonstrate analytically the regions where photochemistry is the dominant process. Whether or not a region may be defined as being in photochemical equilibrium depends on the relative values of the important time constants for ion loss in Saturn's atmosphere: chemical loss (recombination or charge-exchange reactions), diffusive loss (ions diffusing upwards/downwards along Saturn's magnetic field lines), and changes in the electron density peak height h_{max} from meridional wind-driven transport along field lines.

Chemical loss timescales are species dependent and can be approximated by

$$\tau_c \approx \frac{1}{R n_e}, \qquad (9)$$

where R is the fastest chemical loss rate of the dominant ion at a particular altitude. If more than one ion contributes to n_e in Eq. (9), then R is weighted by the ion fractions. Transport timescales for ion–neutral diffusion can be expressed as

$$\tau_d \approx \frac{H^2}{D_a \sin^2 I}, \qquad (10)$$

where H is the atmospheric scale height, D_a is the ion–neutral diffusion coefficient, and I is the magnetic field dip angle (Rishbeth and Garriott, 1969).

Thermospheric meridional winds can cause upward transport along field lines. An important quantifying timescale for this process is the measure of how quickly h_{max} can be shifted vertically by one scale height, or

$$\tau_w \approx \frac{H}{U \sin I \cos I}, \qquad (11)$$

where U is the meridional neutral wind speed (Rishbeth and Garriott, 1969).

Photochemical equilibrium holds when chemical timescales are much smaller than any transport timescales, $\tau_c \ll \tau_d, \tau_w$. Protons ($H^+$) are the dominant ion in Saturn's topside ionosphere, and reaction k_1, the reaction with vibrationally excited H_2, the fastest loss process. At altitudes where H_3^+ is also a major ion, the chemical loss timescale is weighted by its recombination coefficient, α_4. Atmospheric scale heights are on the order of a few hundred kilometers, the ion–neutral diffusion coefficient spans the range from 10^8–10^{13} cm^2 sec^{-1}, and meridional winds reach a maximum of ~ 15 m sec^{-1} for mid-latitude solstice conditions during solar maximum (Müller-Wodarg et al., 2004).

Calculations for mid-latitude (30° N) solar maximum conditions during equinox with these criteria reveal that the conditions for photochemical equilibrium are fulfilled between 1000–2300 km ($\sim 10^{-5}$–10^{-9} mbar), a region that comprises the majority of the ionosphere. Comparisons between modeled profiles with and without diffusion verify these simple predictions. Figure 3a shows a plot of time constants as a function of altitude, where the chemical loss profile τ_c is derived from a diurnally averaged electron density profile. Figure 3b shows ion and electron densities with and without diffusion for 12 LT at 30° N during equinox, solar maximum. The photochemical profile demonstrates excellent agreement with the chemically diffusive profile up to ~ 2300 km. Profiles are plotted in the same manner in Fig. 3c, except for 18 LT at 30° N. Ion densities do not change drastically during the night from those shown in Fig. 3c. Calculations for different latitudes, seasons, and local times can alter the upper boundary of the photochemical regime within Saturn's ionosphere slightly, although never much below 2000 km.
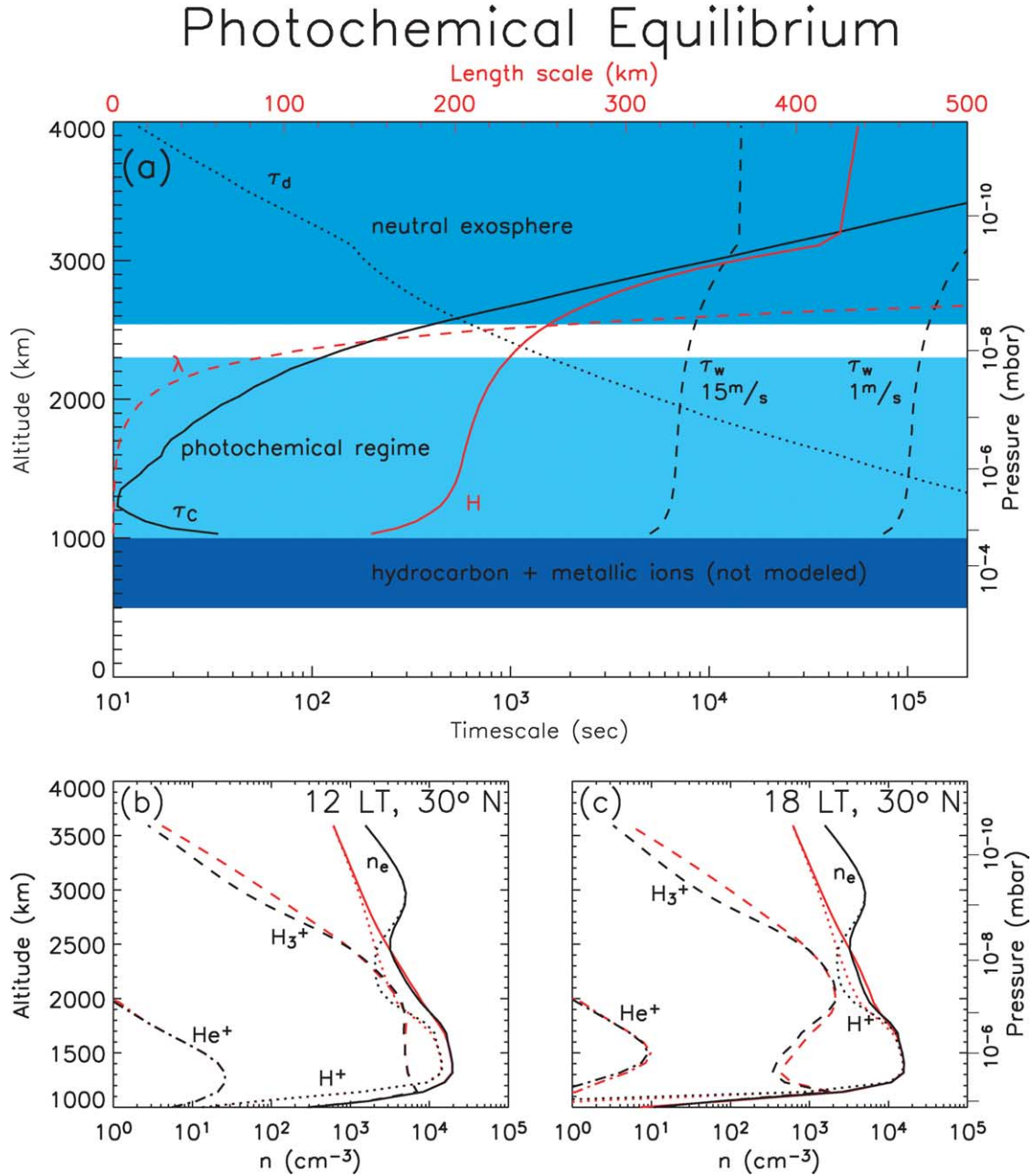
Photochemical Equilibrium

Fig. 3. (a) Comparison of the timescales for ion loss: electron–ion recombination τ_c (solid line), ion–neutral diffusion τ_d (dotted line), and transport from meridional winds τ_w (dashed lines). Two wind speeds have been plotted, describing the full range of meridional winds for mid-latitude solstice conditions (GCM output), 1 and 15 m sec^{-1}. Neutral scale height H and mean free path λ are also plotted, with the lengthscale given on top. The photochemical equilibrium regime is for $\tau_c \ll \tau_d, \tau_w$, and holds between 1000–2300 km, with the neutral exosphere above, and the hydrocarbon and metallic ion regime below. (b) Ion (H$^+$ dotted, H$_2^+$ dashed, He$^+$ dot-dashed) and electron (solid) densities for 12LT at 30° N during equinox. Black curves are for photochemical calculations; red profiles are for calculations with plasma diffusion included. Note that the red and black electron densities are nearly identical below ~ 2300 km. (c) The same as in (b) except for 18LT 30° N during equinox. Calculations for different latitudes and local times reveal that panel (c) is typical of the minimum domain over which photochemical equilibrium holds.

3. Results

3.1. Overview

Electron production in Saturn's ionosphere is due primarily to the photoionization of molecular hydrogen through reactions j_2, j_3, and j_4, all of which are dominated by the 303.8 Å HeII emission line. The photoionization of H$_2^+$ and H$^+$ for overhead illumination as a function of wavelength and altitude is given in Fig. 4. Peak productions occur just below (in altitude) an optical depth of unity. Ionization rates (cm^{-3} sec^{-1}) for reactions j_1, j_2, j_3, and j_4 scale roughly as 1:120:6:2. Thus, there are ~ 20 H$_2^+$ ions produced for every H$^+$ ion (reactions j_1, j_3, and j_4 all produce H$^+$). Profiles
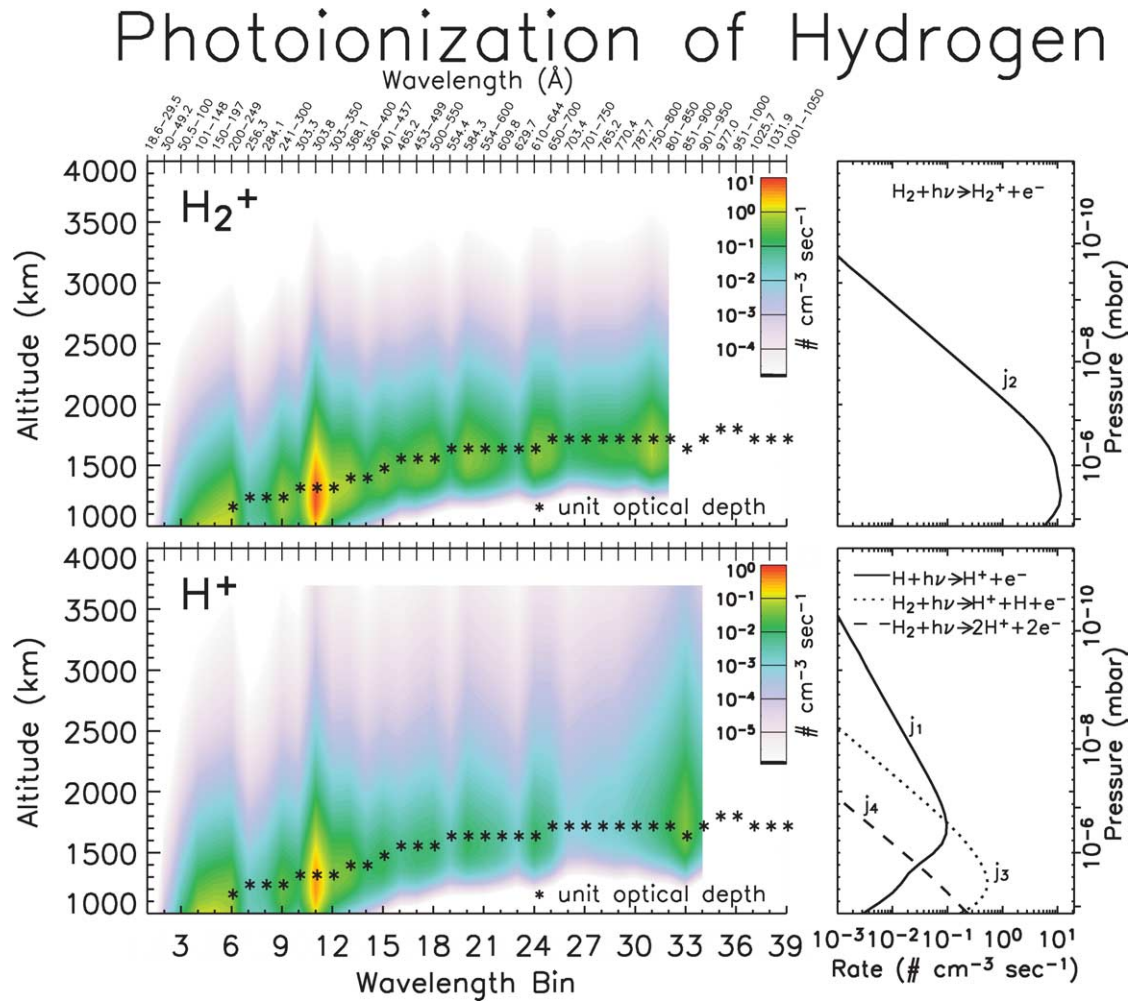
Photoionization of Hydrogen

Fig. 4. Overhead illumination leading to photoproduction of H_2^+ from reaction j_2 (top), and H^+ from reactions j_1, j_3, and j_4 (bottom). The HeII emission line at 303.8 Å (wavelength bin 11) dominates production for reactions j_2 and j_3; the majority of the pure photoionization of H (j_1) comes from photons of wavelength ~ 900 Å. Reaction j_4 is dominated by higher energy photons, primarily those below wavelength bin 6 (i.e., < 200 Å). Asterisks mark altitudes with an optical depth of unity.

of production and loss rates for the important constituents in Saturn's upper ionosphere are given in Fig. 5. Note that nearly all of the H_2^+ produced is immediately lost through the charge exchange reaction with neutral molecular hydrogen, k_3, leading to the production of H_3^+.

Protons (H^+) recombine slowly with electrons (α_1) in Saturn's atmosphere. This fact, coupled with the fast rotation of Saturn, allows for a buildup of H^+ until a steady-state equilibrium is reached, after which there is very little diurnal variation present. H_3^+, a molecular ion, recombines much more quickly (α_4 and α_5) and therefore demonstrates a diurnal variation that closely follows the solar zenith angle. These processes lead to a situation where the daytime ionosphere is dominated by H^+ and H_3^+; H^+ constitutes virtually the entire nighttime ionosphere. Thus, despite H_2^+ being the ion most rapidly produced from solar insolation, it is always a minor ion species.

Radio occultations in Saturn's ionosphere demonstrate jagged electron density profiles, with ill-defined peaks (e.g.,

Waite and Cravens, 1987). The main peak is interpreted to be around 2000–2500 km (Atreya et al., 1984), and the extreme variations below 2000 km are attributed to variable processes such as meteoric influx layers and short-lived hydrocarbon ions (Grebowsky et al., 2002; Moses and Bass, 2000). Photochemical model calculations of ion densities reveal the presence of a double peak in H^+ and hence a double peak in electron density. The photochemical double peak arises from a combination of the three photoionization sources of H^+ (Fig. 4) and the abrupt decrease in the k_1 loss rate above ~ 2500 km (Fig. 5, panel for H^+ loss rates). Specifically, the photoionization rate for reaction j_1 is proportional to [H], while loss due to k_1 is proportional to [H_2]. Thus, combined with the difference between the H and H_2 scale heights, a secondary photochemical regime is defined in the topside with different equilibrium densities. The upper photochemical peak, however, is smoothed out by diffusion, as ions fill the gap between the peaks and flow into the upper ionosphere (Figs. 3b, 3c).
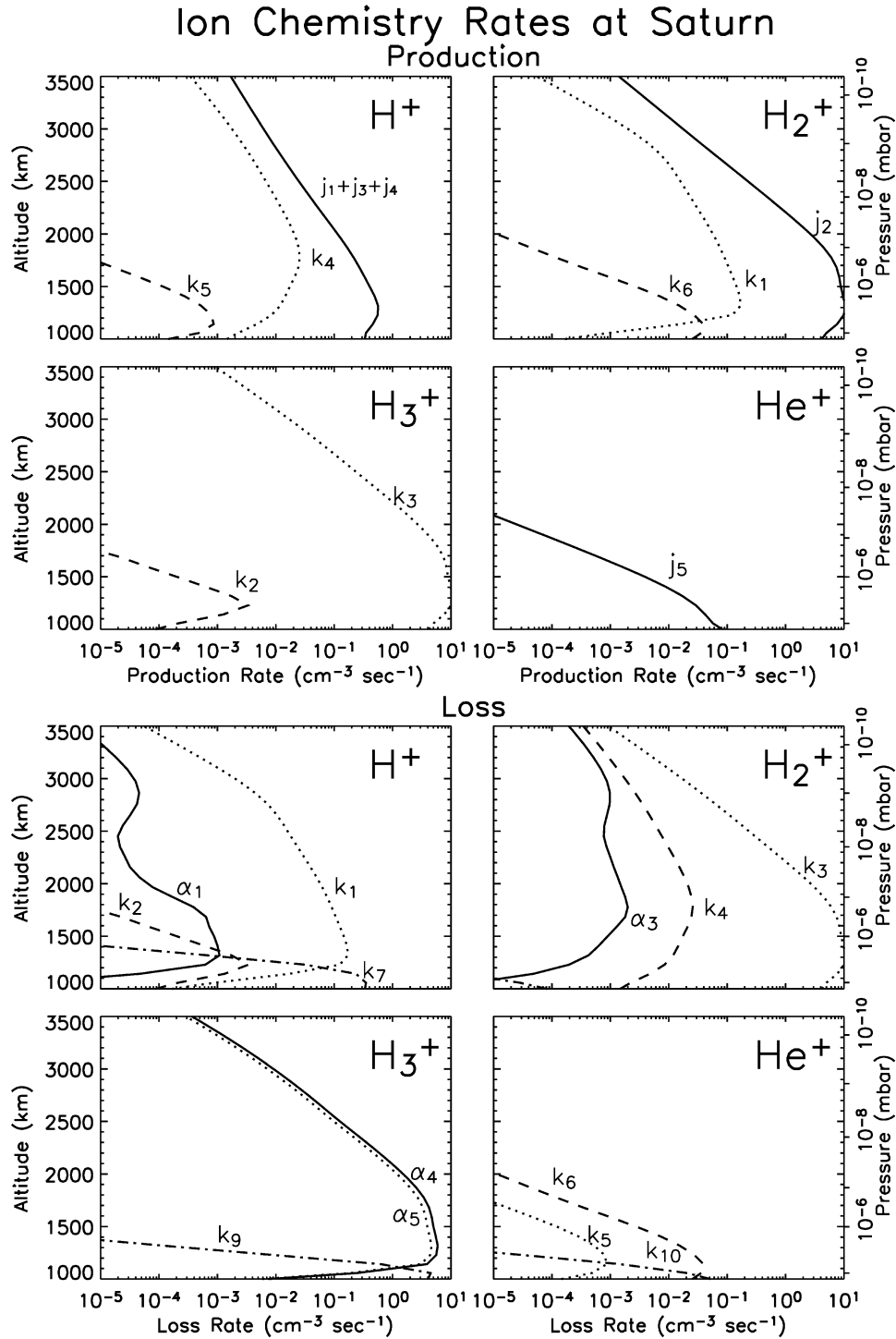
Ion Chemistry Rates at Saturn

Fig. 5. Production (top) and loss (bottom) rates for overhead illumination for a steady-state profile during solar maximum. Each profile is labeled by its reaction from Table 2. Note that no ring shadowing is used in these calculations.

A plot of ion densities at the electron peak versus local time (Fig. 6a) reveals the properties that have been discussed above, namely: strong diurnal variations in H_3^+ that mimic the solar zenith angle and negligible diurnal variations in H^+ that lag the solar zenith angle. A similar plot for 42° N (Fig. 6b) reveals that H_3^+ can actually dominate the ionosphere for a portion of the day, a tendency that becomes more pronounced for smaller solar fluxes (Fig. 6c). Analysis of Eq. (1) for H^+ and H_3^+ under photochemical equilibrium can readily account for this pattern. Assuming $P = L$ for H^+ gives

$$j_3[H_2] \sim k_1[H_2][H^+] \quad \text{or} \quad [H^+] \sim \frac{j_3}{k_1}. \tag{12}$$
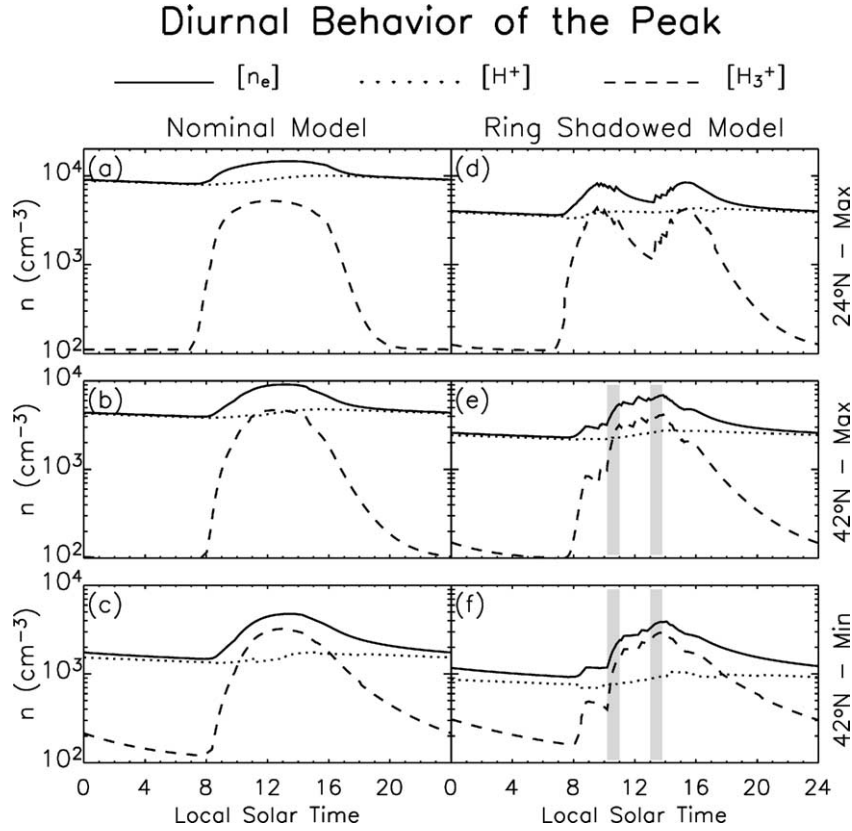
Diurnal Behavior of the Peak

Fig. 6. Diurnal profiles for n_e (solid line), H^+ (dotted line), and H_3^+ (dash–dot line) at the peak of the ionosphere during southern summer. The panels are: (a) 24° N, solar maximum, (b) 42° N, solar maximum, (c) 42° N, solar minimum, (d) 24° N, solar maximum, ring shadowing, (e) 42° N, solar maximum, ring shadowing, and (f) 42° N, solar minimum, ring shadowing. The shaded columns in panels (e) and (f) denote the period of the day when 42° N southern summer passes beneath the Cassini division, and so experiences a brief surge of production over the otherwise shadowed local times (see Fig. 9a).

Similarly, for H_3^+,

$$P_{H_3^+} = k_3[H_2^+][H_2] \sim j_2[H_2]$$

therefore,

$$j_2[H_2] \sim (\alpha_4 + \alpha_5)[H_3^+]n_e \quad \text{or} \quad [H_3^+] \sim \left(\frac{[H_2]}{\alpha_4 + \alpha_5}\right)\frac{j_2}{n_e}. \tag{13}$$

Combining Eqs. (12) and (13),

$$\frac{[H^+]}{[H_3^+]} \sim \left\{\frac{j_3(\alpha_4 + \alpha_5)}{j_2 k_1[H_2]}\right\}n_e. \tag{14}$$

The neutral densities (Fig. 1), and the reaction rates for charge-exchange and recombination (Table 1) are all relatively insensitive to changes in solar flux, while the photoionization rates j_2 and j_3 both scale linearly with solar flux, meaning that the ratio j_3/j_2 is constant. Thus, the $[H^+]/[H_3^+]$ ratio is roughly proportional to the electron density. As solar illumination conditions change, and n_e goes from a higher value to a lower value, the $[H^+]/[H_3^+]$ ratio behaves similarly. This result is borne out in the model calculations and is clearly demonstrated in Fig. 6. The $[H^+]/[H_3^+]$ ratio at noon for 24° N is 1.7 in Fig. 6a. For Fig. 6b the $[H^+]/[H_3^+]$ ratio at noon for 42° N has decreased to 0.92, and the ratio has decreased still further to 0.47 in Fig. 6c, which

represents solar minimum at 42° N. Finally, if ring shadowing is applied to the solar minimum condition at 42° N, then the $[H^+]/[H_3^+]$ ratio is reduced to 0.44 (Fig. 6f).

3.2. Global electron density patterns

A neutral atmosphere that varies across Saturn with latitude and local time is the output of STIM's thermospheric GCM (Müller-Wodarg et al., 2004). By making use of this variable atmosphere a one-dimensional model can yield global ionospheric coverage. Figure 7a shows global maps of peak n_e and h_{max} for southern summer solar maximum. Summer latitudes have peak electron densities between ~ 1.2–2.5×10^4 electrons cm^{-3}, and electron peak heights ranging from ~ 1200 to ~ 1600 km.

Peak density values agree favorably with Voyager and Pioneer radio occultation measurements, while peak heights for most mid-latitudes fall ~ 500–1000 km below those observed (Atreya et al., 1984). Northern winter latitudes show the expected drop-off in n_e and increase in h_{max}, eventually revealing no ionosphere at latitudes that are too deep within the planet's shadow to receive ionizing flux from the Sun. Figure 7c is the equivalent global map for equinox conditions during solar maximum. The same general behavior as seen during solstice is present, with a latitudinal shift in
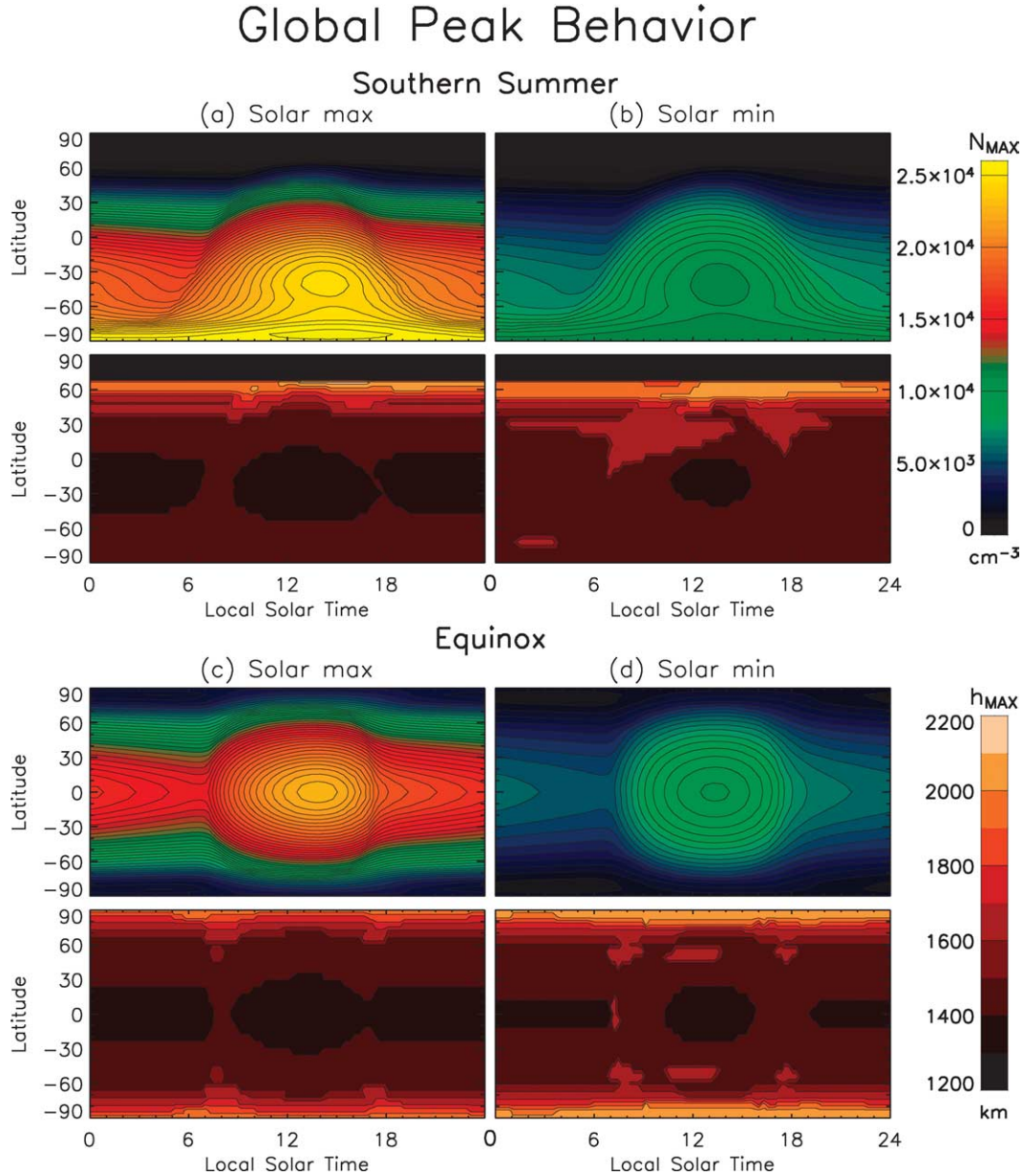
Global Peak Behavior

Southern Summer

Fig. 7. (a) Global contours for peak electron density N_{max} and peak height h_{max} for southern summer solar maximum. Black areas represent portions of Saturn's ionosphere that are never photoionized. (b) Solar minimum, southern summer. (c) Solar maximum, equinox. (d) Solar minimum, equinox. Note that the diurnal peak of N_{max} occurs earlier in the day (~ 1 Saturn hour) during solar minimum. This is due the decrease in the $[H^+]/[H_3^+]$ ratio, as discussed in Section 1.

accordance with the change in solar declination. Solar minimum results during equinox are displayed in Fig. 7d. The decrease in solar flux causes the $[H^+]/[H_3^+]$ ratio to decrease, and therefore, as H_3^+ recombines faster than H^+, the peak electron density occurs earlier in the day (by ~ 1 Saturn hour) than for solar maximum. The decrease in solar flux also leads to a subtle shift of 50–100 km upwards in h_{max} (see Section 3.5).

Vertical integration of an electron density profile $n_e(h)$ (to ~ 4000 km) yields the ionospheric total electron content (TEC). In Saturn's ionosphere, the TEC for solar maximum is 1.5–2×10^{12} cm^{-2} for summer latitudes and 0–2×10^{12} cm^{-2} for winter latitudes (Fig. 8a, where the

zero arises from the fact that northern polar latitudes receive no ionizing flux from the sun during southern summer, and auroral precipitation processes are not included in the model). Panels (b) and (c) in Fig. 8 show the ion components of TEC, i.e., the column contents (N_T) for H^+ and H_3^+ for southern summer solar maximum at four local times. In Fig. 8b, the diurnal variations in H^+ column content match the minimal variations in ion density at the peak (Fig. 6). Similarly, Fig. 8c demonstrates significant diurnal variations in $N_T(H_3^+)$, in agreement with H_3^+ density variations at the peak (Fig. 6). Note that the largest values of $N_T(H^+)$ occur during the afternoon, due to Saturn's fast rotation and the slow loss of $[H^+]$ (Fig. 7).
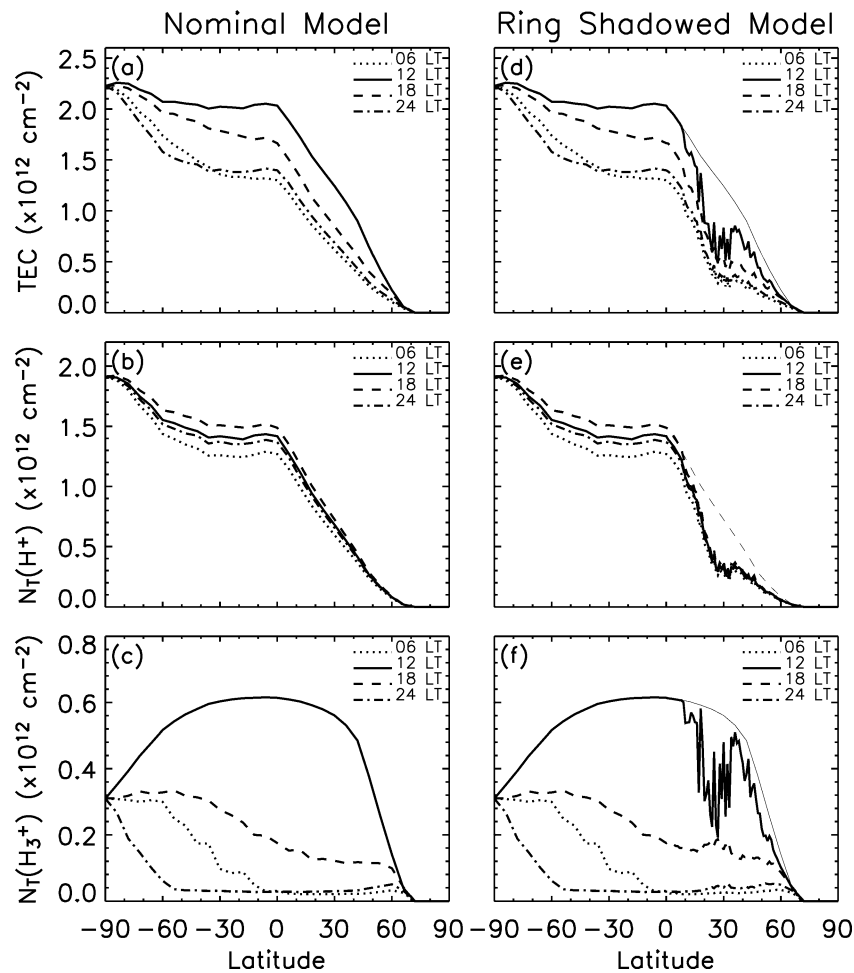
Fig. 8. Total electron (and ion) column content TEC (and N_T) for four different local times as a function of latitude for solar maximum southern summer conditions. The thin lines in panels (d), (e), and (f) represent the non-shadowed peak diurnal values. The jaggedness of the profiles for northern (winter) latitudes of (d), (e), and (f) is a product of ring shadowing (Figs. 2 and 9).

3.3. Ring shadowing

Portions of Saturn's ionosphere that are within the ring shadow will experience attenuation of the incident solar flux. The shadows from the rings during southern summer are displayed as normal optical depth versus latitude and local time in Fig. 9.

Inclusion of the shadow of the rings in the model reduces peak electron densities from non-shadowed model results by as much as a factor of three. Ring-shadowed latitudes also demonstrate slightly higher (50–100 km) peak heights, as a result of the attenuation of solar flux. Furthermore, total column content is reduced drastically at ring-shadowed latitudes. In Fig. 8d, TEC at 24° N latitude has been reduced by a factor of three relative to non-shadowed calculations to 0.5×10^{12} e$^-$ cm^{-2}.

To demonstrate how ring shadowing affects peak density, Figs. 6d, 6e, and 6f show diurnal plots of peak ion densities during southern summer for: 24° N solar maximum, 42° N solar maximum, and 42° N solar minimum. The jagged profiles present in these figures result from different regions of the rings shadowing a particular latitude throughout the

day, causing the solar ion production rate to vary rapidly. Shadowing effects, which include decreased electron densities and increased electron peak altitudes, are clearly visible in Figs. 8d, 8e, 8f, and 9, which show considerably altered global maps of TEC, and n_e and h_{max}, respectively, for southern summer solar maximum.

Attenuation of solar flux by the rings is found to be strongly dependent on the solar declination, as is latitudinal coverage of the ring shadows. This is a result of the geometry of the system; as the rings traverse from a tilted inclination to an edge-on inclination, the UV absorption of the rings will increase drastically (thicker absorbing medium) and the resultant shadow will decrease in size (smaller shadowing object).

An important aspect of the ring model used in this study is the presence of the Cassini division, which allows more than 80% of incident sunlight to reach the ionosphere. The gap manifests itself clearly in Fig. 9b as an arc of relatively large electron densities, and has the effect of allowing otherwise shadowed latitudes to be illuminated by ionizing sunlight for brief portions of the day (15 min to 2–3 hr). Figures 6e and 6f provide apt demonstrations of this surge in production, as
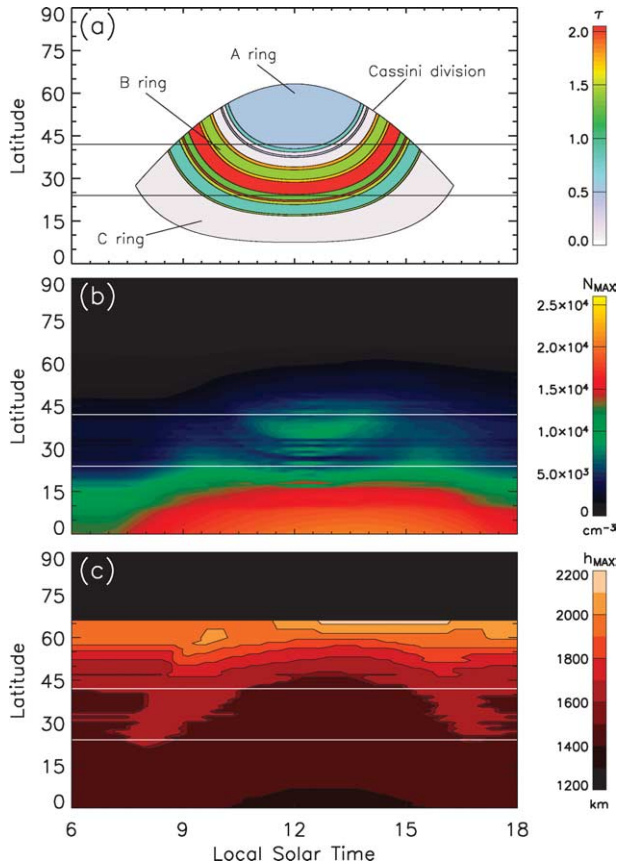
Fig. 9. (a) Global ring shadowing distribution for southern summer, given in normal optical depths. Around 10 and 13 LT, 42° N passes through the Cassini gap, and so experiences minimal attenuation of solar flux. (b) N_{max} distribution for northern latitudes during solar maximum southern summer. Significant deviation from the unshadowed distribution (Fig. 7a) is evident. (c) Same as (b), except h_{max}. Note that the reduction in solar flux (due to ring shadowing) has raised h_{max} values slightly from those in Fig. 7a (as discussed in Section 3.3). Diurnal electron and ion profiles at the peak for the altitudes designated by horizontal lines (24° N and 42° N) are given in Fig. 6.

sharp rises in electron and ion densities are visible around 10 and 13 LT (the shaded columns), just when 42° N latitude passes through the Cassini gap during southern summer (see Fig. 9a). Without this respite from attenuated sunlight, Saturn's ionosphere would contain lower electron densities throughout the shadowed region.

Finally, ring shadowing could play a role in a host of other effects in Saturn's ionosphere, e.g., equatorial "fountain" effects, and H^+ outflow from the conjugate hemisphere to the ring-shadowed hemisphere due to shadow-induced pressure gradients (Waite, 1981).

3.4. Diurnal variations

By applying ad hoc alterations to the rate (k_1) of the reaction between H^+ and vibrationally excited H_2 it is possible to span completely the range from an atomic ion regime to a molecular ion regime, as a larger k_1 results in less H^+, more H_2^+, and consequently more H_3^+. Table 2 gives a sum-

mary of these variations, where all calculations have been performed for 30° N equinox during solar maximum. Increasing k_1 past its nominal rate will not affect the peak electron density, but it will alter the ion mixing ratios by weighting H_3^+ more heavily. Decreasing k_1 *will* cause a net increase in electron density, as this allows for a higher proportion of H^+ ions, which, combined with the now slower loss process for H^+, means equilibrium requires larger electron densities. Reductions in k_1 by a factor of 10^4 or more essentially remove the reaction, and result in an entirely atomic ion regime with a constant peak density of order 10^5 cm^{-3} (Table 2, Test #2), in agreement with early model predictions (McElroy, 1973; Atreya and Donahue, 1975; Capone et al., 1977; Waite, 1981). An increase by a factor of $\geqslant 10^2$ yields an entirely molecular ion regime with a peak density of $\sim 10^4$ cm^{-3} (Table 2, Test #4). Increasing k_1 by a factor of five induces enough diurnal variation to match the SED-inferred midnight electron density minimum at $\sim 10^3$ cm^{-3}; however dawn/dusk densities are then too low to match observations (2–5 × 10^3 cm^{-3}), and densities at noon are only $\sim 1.2 \times 10^4$ cm^{-3} (Table 2, Test #3). These results agree well with the calculated variations induced in Jupiter's ionosphere due to variations in the k_1 reaction rate (McConnell et al., 1982).

The k_1 reaction rate should vary as conditions for H_2 excitation change, although most likely not by the four orders of magnitude discussed here—and especially not over the course of one Saturn day (10.7 hr). Additionally, diurnal temperature variations in the thermosphere are predicted to be very small—on the order of several degrees (Müller-Wodarg et al., 2004)—meaning that any variation in the excited H_2 population due to temperature is also extremely minimal. Thus, by choosing two different values for the k_1 rate, the model can match the diurnal *extremes* derived from the SED measurements, although there is no one value that will match both extremes within the same day (i.e., the full diurnal *variation*), so other processes would be needed to explain the suggested large diurnal changes.

Inclusion of water chemistry in the model allows for one more parameter that can affect diurnal variations in electron density. Moses and Bass (2000) consider three sources of water flux in Saturn's ionosphere: micrometeoroid ablation in the 790–1300 km altitude region at a rate of 1.5×10^6 molecules cm^{-2} sec^{-1} (method A), ring-derived flux entering the top of the atmosphere at a rate of 1.5×10^6 molecules cm^{-2} sec^{-1} (method B), and an enhanced ring-derived flux at a rate of 1.0×10^8 molecules cm^{-2} sec^{-1} (method C). Water fluxes for methods A and B produce mixing ratios that are consistent with the Infrared Space Observatory (ISO) measurements (Feuchtgruber et al., 1997), and these fluxes are an order of magnitude smaller than the fluxes used previously to explain the peak of Saturn's ionosphere (Majeed and McConnell, 1991, 1996; Connerney and Waite, 1984).

As a test of ion loss due to water influx, STIM was modified to incorporate the mixing ratio profiles for H_2O given in Fig. 9b of Moses and Bass (2000), which are recalcula-

Table 2
Diurnal variations in peak electron density: 30° N equinox solar maximum

Test #	k_1 fraction	H_2O flux method[a]	06 LT n_e ($\times 10^3$ cm^{-3})	12 LT n_e ($\times 10^3$ cm^{-3})	18 LT n_e ($\times 10^3$ cm^{-3})	24 LT n_e ($\times 10^3$ cm^{-3})
1	1	None	13	19	16	14
2	10^{-4}	None	160	160	160	160
3	5	None	2.0	12	6.0	3.0
4	100	None	1.0	11	3.9	1.6
5	1	A	6.9	14	9.9	7.8
6	1	B	5.4	13	8.6	6.2
7	1	C	1.0	7.8	3.8	1.3
8	0	A	38	40	40	39
9	0	B	29	31	30	29
10	0	C	1.4	7.8	3.8	1.7
11	0	None	0.85	12	_[b]	1
12	5	C	_[b]	100	11	7.2

[a] Moses and Bass (2000), where A: micrometeoroid ablation in 790–1300 km region at 1.5×10^6 molecules cm^{-2} sec^{-1}; B: ring-derived flux entering top of atmosphere at 1.5×10^6 molecules cm^{-2} sec^{-1}; C: ring-derived flux entering top of atmosphere at 1.0×10^8 molecules cm^{-2} sec^{-1}.

[b] Calculations are only for half a Saturn day.

tions of the photochemically diffusive profiles from Moses et al. (2000) for different solar fluxes. The mixing ratios are then applied to self-consistent thermospheric GCM calculations to determine H_2O concentrations. Despite H_2O not being included in the GCM calculations, the minute values of the mixing ratios ($< 10^{-6}$) should not affect the accuracy of the GCM atmosphere.

Table 2 gives results from several H_2O flux scenarios. It is clear that the first two ring fluxes have very little influence on the diurnal electron density when introduced into the nominal model where the k_1 reaction rate is unchanged (Tests #5 and #6). The Method C flux, representing a ring influx for latitudes connected magnetically to regions of enhanced ring erosion (Connerney and Waite, 1984), reduces densities enough to match the midnight value of $\sim 10^3$ cm^{-3}, but the dawn/dusk densities are too low ($1–4 \times 10^3$ cm^{-3}) to match observations (Table 2, Test #7). None of these water flux calculations can produce a larger density at noon, they are loss processes only.

In order to fully explore the effects of water chemistry in Saturn's ionosphere calculations are also performed with the k_1 reaction rate set to zero. In this scenario H_2O reactions are the dominant loss for H^+. The inclusion of different fluxes of water in the photochemical model leads to the same behavior as varying the k_1 reaction rate. Namely, larger fluxes provide more chemical loss for H^+ and therefore shift Saturn's ionosphere nearer to a molecular ion regime with larger diurnal variation. Without a drastic water flux, the loss of H^+ from chemical reactions with H_2O is not enough to allow for strong diurnal variations in n_e. Even allowing for an extreme flux, the maximum diurnal pattern in modeled n_e (~ 4.6 noon-to-midnight; Table 2, Test #10) fails to come close to the SED-inferred variations (~ 100 noon-to-midnight).

If these loss processes assumed the extreme variations described above, it would still not be possible within the ionospheric model to traverse the drastic minimum and maximum electron densities inferred from SED observa-

tions within one Saturn day. Midnight densities of 10^3 electrons cm^{-3} will only reach 1.2×10^4 electrons cm^{-3} by noon with $k_1 = k_{11-14} = 0$ (i.e., recombination being the only loss; Table 2, Test #11). With k_1 increased by a factor of 5 and an enhanced water flux from the rings (method C), noontime densities of 10^5 electrons cm^{-3} have decreased to 7.2×10^3 electrons cm^{-3} by midnight (Table 2, Test #12). Using less dramatic loss processes, however, electron densities fail to decrease below 10^4 electrons cm^{-3} by midnight. Thus, even by varying these two parameters throughout a Saturn day (k_1 reaction rate and H_2O influx), the model cannot reproduce the changes in diurnal electron concentrations derived from SED measurements. Other modifications to the ionosphere—such as transport—must play a role if SED diurnal variations are to be successfully modeled.

3.5. Peak height of the ionosphere

As mentioned in Section 1, radio occultation observations measured dawn/dusk electron density profiles with peak heights between 1900–2900 km (Atreya et al., 1984). Model calculations without the k_1 or k_{11} reactions predict an H^+ dominated ionosphere with peak heights at around 1200 km (e.g., Atreya et al., 1984). The introduction of the k_1 and k_{11} reactions tends to (in addition to affecting N_{max}, Table 2) raise h_{max} (Connerney and Waite, 1984; Majeed and McConnell, 1991; Moses and Bass, 2000).

In this study, nominal model calculations—where k_1 is given by Eq. (7), and $[H_2O] = 0$ cm^{-3}—demonstrate peak electron densities in agreement with observations, but peak heights at mid-latitudes are 500–1000 km below those observed. However, by introducing H_2O into the atmosphere and reducing the k_1 reaction rate simultaneously, it is possible to reproduce the observed dawn/dusk electron densities while also increasing the peak height to ~ 2000 km at mid-latitudes. Calculations for 30° N equinox during solar maximum with a ring-derived H_2O influx (method B) and the k_1 reaction rate reduced by a factor of 10^3 produce an

ionosphere with $N_{\max} \sim 10^4$ cm^{-3} and $h_{\max} \sim 2000$ km. In addition, such a profile has a larger plasma scale height (~ 1000 km) and an electron density of order 10^3 cm^{-3} at 4000 km, a good match to some (but not all) of the radio occultations (Atreya et al., 1984). The peak heights and electron density altitude profiles might be further altered by accounting for distortions of the atmosphere from Saturn's rotation (an effect that peaks at the equator and is zero at the pole).

As the observations are sparse and widely varying, the reaction rate for k_1 is ill constrained, the diurnal variations in n_e are controversial, and the global distribution of H_2O influx is unknown, it is difficult at this point in time to justify such variations in parameter space beyond the nominal model. Instead, this task remains a subject of future study, one that will surely benefit from a robust set of $n_e(h)$ profiles provided by Cassini.

3.6. Pedersen conductivities

Plasma flow patterns in Saturn's magnetosphere result from a blend of solar-wind-induced and corotationally imposed motions of flux tubes. As described recently by Bunce et al. (2003), Cowley et al. (2004), and Cowley and Bunce (2004), one of the key parameters in need of specification is the effective height-integrated Pedersen conductivity (Σ_P^*) for Saturn's high latitude ionosphere. As Cowley et al. (2004) point out, values obtained from observed and modeled electron density profiles range from ~ 0.1 to ~ 100 mho (Connerney et al., 1983; Atreya et al., 1984; Cheng and Waite, 1988). Isbell et al. (1984) used a value of 10 mho in their discussion of rigid corotation effects; Bunce et al. (2003) argue for values of ~ 1–2 mho as an upper limit to account for sub-corotation near $\sim 8R_S$ on the dayside (geomagnetic dipole latitude of $\sim 70°$). While Σ_P calculations (from observed profiles) and predictions (from models) differ from the upper limit imposed by Bunce et al. (2003), this difference is accounted for by a correction factor that represents slippage of the neutral atmosphere due to ion–neutral frictional drag (Huang and Hill, 1989). As expressed by Cowley and Bunce (2004), the effective height-integrated Pedersen conductivity is

$$\Sigma_P^* = (1 - k)\Sigma_P, \tag{15}$$

where k is the correction factor and assumes a value between 0 and 1. Preliminary results from the JIM model of the coupled jovian ionosphere–thermosphere indicate that k may be as large as ~ 0.5 for Jupiter (Bunce and Cowley, 2001).

Model calculations from this study are displayed in Fig. 10, which gives diurnal plots of height-integrated Pedersen conductivities at high latitude for southern summer and equinox during solar maximum. For $70°$ S latitude at noon the integrated Pedersen conductivity Σ_P is 18 mho (equinox) and 42 mho (summer solstice). These profiles display a diurnal variation of ~ 3, whereas previous estimates by Cheng and Waite (1988) have a variation of ~ 50
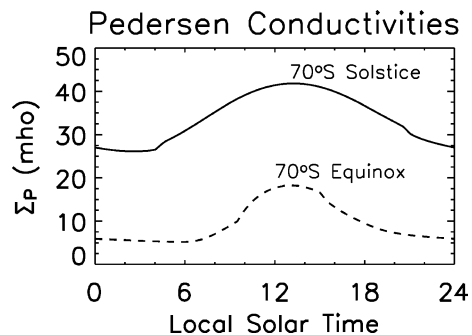

Fig. 10. Model calculation of height-integrated Pedersen conductivities Σ_P for southern summer (solid) and equinox (dashed) at $70°$ magnetic latitude. Note that these results pertain to photochemical sources of conductivity only (see Section 3.6).

and a peak Σ_P of 260 mho. Cheng and Waite (1988) used occultation measurements of $n_e(h)$ along with the SED-inferred $N_{\max}$ variation to make their calculations; therefore the differences in calculated diurnal variations of Σ_P between Cheng and Waite (1988) values and STIM values result simply from differences in the two diurnal variations of ionospheric densities.

It should be stressed that the ionospheric model does not include auroral production of plasma and thus pertains to solar sources of conductivity only. In addition, hydrocarbon ions are not modeled and therefore the ion density below the homopause is under-predicted. Using the ion profiles from Fig. 4a of Moses and Bass (2000) with the neutral atmosphere from the GCM to calculate conductances, the hydrocarbon ions (predominately $C_3H_5^+$) account for only 0.1 of 9.5 mho. This is because $C_3H_5^+$ is the dominant source of conductivity below ~ 1000 km (with an average of $\sim 7 \times 10^{-9}$ mho m^{-1}), but H^+ and H_3^+ are the dominant sources of conductivity above 1000 km (they average $\sim 3.5 \times 10^{-6}$ mho m^{-1}). Thus, hydrocarbon ions contribute in only a minor way to the total conductance, and Fig. 10 is representative of the total photochemically produced conductance at Saturn. These results are in agreement with Cheng and Waite (1988), who found that calculations for Pedersen conductance at Saturn using radio occultation measurements were insensitive to the low-lying ionospheric layers.

4. Conclusions

A one-dimensional time-dependent model of Saturn's ionosphere has been developed and has been sequentially coupled to a global circulation model of the thermosphere in order to provide three-dimensional coverage of the thermosphere–ionosphere system. It has been shown that the assumption of photochemical equilibrium is valid throughout the majority (~ 1000–2300 km) of the ionosphere of Saturn. Comparisons with previous 1-D modeling efforts (Moses and Bass, 2000; Majeed and McConnell, 1996, 1991) reveal excellent agreement both qualitatively and

quantitatively; the model results offered here thus extend prior studies into two additional dimensions with the benefit of a self-consistent thermospheric GCM.

Photoionization in Saturn's ionosphere is dominated by the HeII line at 303.8 Å. Relative ion fractions of the dominant ions determine the diurnal behavior of the electron density: essentially no diurnal variation for an atomic regime (H^+) and a strong diurnal variation that mirrors the solar zenith angle for a molecular ionosphere (H_3^+). The ion fractions vary with height and their dependence on solar flux conditions is described for the first time, with the $[H^+]/[H_3^+]$ ratio being larger for larger fluxes. H^+ is the dominant ion under most conditions, although for low incident sunlight H_3^+ becomes dominant near the peak for a majority of the day. Therefore, Saturn's ionosphere cannot be categorized as entirely molecular or atomic; both are possible depending on conditions at Saturn.

Shadowing by the rings of Saturn has been explored for the first time and is found to significantly reduce predicted electron densities. During southern summer, the season for Cassini's arrival at Saturn, shadowed latitudes in the northern hemisphere show electron densities and total electron content depressed by as much as a factor of three. Other seasons will display more drastic reductions, although over more limited latitude ranges. The Cassini Division plays the important role of allowing brief periods of (nearly) unattenuated sunlight for otherwise shadowed regions, and without its presence modeled electron densities would be significantly reduced.

Calculations were performed to explore the full range of electron and ion densities for Saturn's ionosphere, depending on the variations of the two dominant loss processes for H^+ (charge-exchange with vibrationally excited H_2 and charge-exchange with H_2O). Just as with recent models (Moses and Bass, 2000; Majeed and McConnell, 1996, 1991), the most likely conditions for the two losses give peak dawn/dusk electron densities of $\sim 10^4$ cm^{-3}, in agreement with observations. Calculations in this study reveal a peak height at mid-latitudes considerably lower than observed h_{max}, however variations in the k_1 reaction rate and the influx of H_2O into the top of the atmosphere can shift the peak height upwards by a few hundred kilometers, as pointed out earlier by Connerney and Waite (1984).

Electron densities inferred from Voyager SED measurements implied a diurnal variation of two orders of magnitude, from $\sim 10^3$ to 10^5 electrons cm^{-3}. Model calculations with electron–ion recombination as the only loss for H^+ yield an atomic ionosphere at 10^5 electrons cm^{-3} with no diurnal variation. By increasing the nominal reaction rate for H^+ and vibrationally excited H_2, or by allowing an enhanced influx of water from the ring system (1.0×10^8 molecules cm^{-2} sec^{-1}), it is possible to model midnight electron densities of a few times 10^3 electrons cm^{-3}, but noon values for those same parameters will not exceed 10^4 electrons cm^{-3}. Thus, there is no set of parameters that will combine to model the SED *diurnal* profile. Moreover, it has been shown that it is physically impossible to traverse two orders of magnitude in electron density twice in a Saturn day with the model, even under the most drastic of conditions.

Model calculations of height-integrated Pedersen conductivity for photochemical sources of ionization give peak values of 18 mho for 70° S equinox and 42 mho for 70° S southern summer, indicating that the correction factor k, representing slippage of the neutral atmosphere due to ion–neutral frictional drag, is > 0.6, and may be as large as 0.95.

Considerable progress in understanding Saturn's ionosphere has been made since the Voyager and Pioneer spacecraft first made measurements, more than twenty years go. The data from Cassini will build upon that knowledge by providing the observations necessary to constrain and validate theory for Saturn's coupled thermosphere–ionosphere system.

Note added in proof

Newer versions of the SOLAR2000 model released recently (v2) show different solar fluxes than the older version used in this study, v1.23. In particular, the X-ray fluxes are higher and the HeII line at 303.8 Å no longer dominates the spectrum. Calculations with the more recent solar fluxes reveal different quantitative results than those quoted here; however, the qualitative behaviors discussed remain the same with the exception of the dominance of the HeII line in photoionization. In general, model calculations with the new solar fluxes find an ionosphere with the electron density reduced by a factor of ~ 2 when all other conditions remain the same.

Appendix A

Photoionization and photoabsorption cross-sections[a]

Bin	λ_i (Å)	λ_f (Å)	j_1[b]	j_2[c]	j_3[c,d]	j_4[c,d]	j_5[e]	$H_{2\,abs}$[f]
1	18.6	29.5	1.31×10^{-4}	2.65×1^{-4e}	0	1.0×10^{-6g}	3.14×10^{-3}	0
2	30	49.2	5.86×10^{-4}	1.27×10^{-3e}	0	1.0×10^{-5g}	0.0148	0
3	50.5	100	4.02×10^{-3}	8.38×10^{-3e}	0	2.0×10^{-4g}	0.1	0
4	100.5	148.4	0.0182	0.0357	0[g]	2.3×10^{-3}	0.402	0
5	150.1	198.6	0.05	0.116	1.00×10^{-4g}	5.3×10^{-3}	0.927	0

Appendix A (*continued*)

Bin	λ_i (Å)	λ_f (Å)	j_1[b]	j_2[c]	j_3[c,d]	j_4[c,d]	j_5[e]	$H_{2\,abs}$[f]
6	200	249.2	0.107	0.281	0.01	3.8×10^{-3}	1.64	0
7	256.3	–	0.159	0.465	0.022	1.0×10^{-3}	2.17	0
8	284.1	–	0.216	0.627	0.03	8.0×10^{-5}	2.68	0
9	251.1	299.5	0.197	0.605	0.027	1.0×10^{-4}	2.51	0
10	303.3	–	0.263	0.805	0.042	4.0×10^{-5}[g]	3.05	0
11	303.8	–	0.264	0.805	0.042	4.0×10^{-5}[g]	3.06	0
12	303.3	349.9	0.329	1.1	0.0525	1.0×10^{-5}[g]	3.53	0
13	368.1	–	0.47	1.57	0.072	2.0×10^{-6}[g]	4.43	0
14	356	399.8	0.509	1.68	0.0735	1.0×10^{-6}[g]	4.65	0
15	401.1	436.7	0.693	2.56	0.0853	0[g]	5.56	0
16	465.2	–	0.95	3.52	0.086	0	6.57	0
17	453	499.4	1.02	3.79	0.0873	0	6.81	0
18	500	550	1.36	5	0.103	0	1.36	0
19	554.4	–	1.61	5.59	0.11	0	0	0
20	584.3	–	1.88	6.44	0.12	0	0	0
21	554.4	599.6	1.81	6.26	0.12	0	0	0
22	609.8	–	2.14	7.04	0.15	0	0	0
23	629.7	–	2.36	7.74	0.14	0	0	0
24	609.8	644.1	2.32	7.51	0.145	0	0	0
25	650.3	700	2.9	9.24	0.0918	0	0	0
26	703.4	–	3.28	11.3	0.0100[g]	0	0	0
27	701	750	3.6	12.2	0[g]	0	0	0
28	765.2	–	4.23	10.6	0	0	0	0
29	770.4	–	4.31	9.6	0	0	0	0
30	787.7	–	4.61	7.7	0	0	0	4
31	750	800	4.39	10	0	0	0	0
32	801	850	5.31	2	0	0	0	8
33	851	900	6.33	0	0	0	0	8.05
34	901	950	1.55	0	0	0	0	12
35	977.0	–	0	0	0	0	0	18.5
36	951	1000	0	0	0	0	0	18.5
37	1025.7	–	0	0	0	0	0	13
38	1031.9	–	0	0	0	0	0	11
39	1001	1050	0	0	0	0	0	13

[a] Cross-sections are given in units of Mb; i.e., 10^{-18} cm^{-2}.
[b] Samson (1966).
[c] Chung et al. (1993).
[d] Dujardin et al. (1987).
[e] Yan et al. (1998).
[f] Backx et al. (1976).
[g] Extrapolated from reference.

Acknowledgments

References

Anicich, V.G., 1993. Evaluated bimolecular ion-molecule gas phase kinetics of positive ions for use in modeling planetary atmospheres, cometary comae, and interstellar clouds. J. Phys. Chem. Ref. Data 22, 1469–1569.

Atreya, S.K., Donahue, T.M., 1975. Ionospheric models of Saturn, Uranus, and Neptune. Icarus 24, 358–362.

Atreya, S.K., Waite, J.H., Donahue, T.M., Nagy, A.F., McConnell, J.C., 1984. Theory, measurements and models of the upper atmosphere and ionosphere of Saturn. In: Gehrels, E. (Ed.), Saturn. Univ. of Arizona Press, Tucson, pp. 239–277.

Backx, C., Wight, G.R., Van der Wiel, M.J., 1976. Oscillator strengths (10–70 eV) for absorption, ionization and dissociation in H2, HD and D2, obtained by an electron–ion coincidence method. J. Phys. B 9, 315–331.

Brinkman, A.W., McGregor, J., 1979. The effect of the ring system on the solar radiation reaching the top of Saturn's atmosphere: direct radiation. Icarus 38, 479–482.

Broadfoot, A.L., Sandel, B.R., Shemansky, D.E., Holberg, J.B., Smith, G.R., Strobel, D.F., McConnell, J.C., Kumar, S., Hunten, D.M., Atreya, S.K., Donahue, T.M., Moos, H.W., Bertaux, J.L., Blamont, J.E., Pomphrey, R.B., Linick, S., 1981. Extreme ultraviolet observations from Voyager 1 encounter with Saturn. Science 212, 206–211.

Bunce, E.J., Cowley, S.W.H., 2001. Divergence of the equatorial current in the dawn sector of Jupiter's magnetosphere: analysis of Pioneer and Voyager magnetic field data. Planet. Space Sci. 49, 1089–1113.

Bunce, E.J., Cowley, S.W.H., Wild, J.W., 2003. Azimuthal magnetic fields in Saturn's magnetosphere: effects associated with plasma sub-corotation and the magnetopause-tail current system. Ann. Geophys. 21, 1709–1722.

Capone, L.A., Whitten, R.C., Prasad, S.S., Dubach, J., 1977. The iono-spheres of Saturn, Uranus, and Neptune. Astrophys. J. 215, 977–983.

Cheng, A.F., Waite Jr., J.H., 1988. Corotation lag of Saturn's mag-netosphere: global ionospheric conductivities revisited. J. Geophys. Res. 93, 4107–4109.

Chung, Y.M., Lee, E.-M., Masuoka, T., Samson, J.A.R., 1993. Dissociative photoionization of H_2 from 18 to 124 eV. J. Chem. Phys. 99, 885–889.

Connerney, J.E.P., Waite Jr., J.H., 1984. New model of Saturn's ionosphere with an influx of water from the rings. Nature 312, 136–138.

Connerney, J.E.P., Acuña, M.H., Ness, N.F., 1983. Currents in Saturn's magnetosphere. J. Geophys. Res. 88, 8779–8789.

Cowley, S.W.H., Bunce, E.J., 2004. Corotation-driven magnetosphere–ionosphere coupling currents in Saturn's magnetosphere and their re-lation to the auroras. Ann. Geophys. 21, 1691–1707.

Cowley, S.W.H., Bunce, E.J., Prangé, R., 2004. Saturn's polar ionospheric flows and their relation to the main auroral oval. Ann. Geophys. 22, 1379–1394

Cravens, T.E., 1987. Vibrationally excited molecular hydrogen in the upper atmosphere of Jupiter. J. Geophys. Res. 92, 11083–11100.

Doyle, T.H., Feldman, P.D., Holberg, J.B., McGrath, M.A., 1996. Fluores-cent hydroxyl emissions from Saturn's ring atmosphere. Science 272, 516–518.

Dujardin, G., Besnard, M.J., Hellner, L., Malinovitch, Y., 1987. Double photoionization of H_2: an experimental test of electronic-correlation models in molecules. Phys. Rev. A 35, 5012–5019.

Esposito, L.W., O'Callaghan, M., Simmons, K.E., Hord, C.W., West, R.A., Lane, A.L., Pomphrey, R.B., Coffeen, D.L., Sato, M., 1983. Voy-ager photopolarimeter stellar occultation of Saturn's rings. J. Geophys. Res. 88, 8643–8649.

Feuchtgruber, H., Lellouch, E., de Graauw, T., Bézard, B., Encrenaz, T., Griffin, M., 1997. External supply of oxygen to the atmospheres of the giant planets. Nature 389, 159–162.

French, R.G., Nicholson, P.D., 2000. Saturn's rings II: particle sizes inferred from stellar occultation data. Icarus 145, 502–523.

Gladstone, G.R., Yelle, R.V., Majeed, R., 2002. Solar System upper atmospheres: photochemistry, energetics and dynamics. Geophysical Monograph, vol. 130. American Geophysical Union, Washington, DC, pp. 23–37.

Grebowsky, J.M., Moses, J.I., Pesnell, W.D., 2002. Meteoric material—an important component of planetary atmospheres. Geophysical Mono-graph, vol. 130. American Geophysical Union, Washington, DC, pp. 235–244.

Holberg, J.B., Forrester, W.T., Lissauer, J.J., 1982. Identification of reso-nance features within the rings of Saturn. Nature 297, 115–120.

Huang, T.S., Hill, T.W., 1989. Corotation lag of the jovian atmosphere, ionosphere, and magnetosphere. J. Geophys. Res. 94, 3761–3765.

Isbell, J., Dessler, A.J., Waite Jr., J.H., 1984. Magnetospheric energization by interaction between planetary spin and the solar wind. J. Geophys. Res. 89, 10716–10722.

Kaiser, M.L., Desch, M.D., Connerney, J.E.P., 1984. Saturn's ionosphere: inferred electron densities. J. Geophys. Res. 89, 2371–2376.

Kim, Y.H., Fox, J.L., 1994. The chemistry of hydrocarbon ions in the jovian ionosphere. Icarus 112, 310–325.

Majeed, T., McConnell, J.C., 1991. The upper ionospheres of Jupiter and Saturn. Planet. Space Sci. 39, 1715–1732.

Majeed, T., McConnell, J.C., 1996. Voyager electron density measurements on Saturn: analysis with a time dependent ionospheric model. J. Geo-phys. Res. 101, 7589–7598.

Majeed, T., McConnell, J.C., Yelle, R.V., 1990. Vibrationally excited H_2 in the upper atmosphere of Saturn. Adv. Space Res. 10, 131–134.

Majeed, T., McConnell, J.C., Yelle, R.V., 1991. Vibrationally excited H_2 in the outer planets thermosphere: fluorescence in the Lyman and Werner bands. Planet. Space Sci. 39, 1591–1606.

Marouf, E.A., Tyler, G.L., Zebker, H.A., Simpson, R.A., Eshleman, V.R., 1983. Particle size distributions in Saturn's rings from Voyager 1 radio occultation. Icarus 54, 189–211.

Marouf, E.A., Tyler, G.L., Rosen, P.A., 1986. Profiling Saturn's rings by radio occultation. Icarus 68, 120–166.

Maurellis, A.N., 1998. Non-auroral models of the jovian ionosphere. The-sis. Univ. of Kansas, Lawrence.

Maurellis, A.N., Cravens, T.E., 2001. Ionospheric effects of Comet Shoemaker–Levy 9 impacts with Jupiter. Icarus 154, 350–371.

McConnell, J.C., Holberg, J.B., Smith, G.R., Sandel, B.R., Shemansky, D.E., Broadfoot, A.L., 1982. A new look at the ionosphere of Jupiter in light of the UVS occultation results. Planet. Space Sci. 30, 151–167.

McElroy, M.B., 1973. The ionospheres of the major planets. Space Sci. Rev. 14, 460–473.

Millar, T.J., Farquhar, P.R.A., Willacy, K., 1997. The UMIST database for astrochemistry 1995. Astron. Astrophys. Suppl. Ser. 121, 139–185.

Moses, J.I., Bass, S.F., 2000. The effects of external material on the chem-istry and structure of Saturn's ionosphere. J. Geophys. Res. 105, 7013–7052.

Moses, J.I., Bézard, B., Lellouch, E., Gladstone, G.R., Feuchtgruber, H., Allen, M., 2000. Photochemistry of Saturn's atmosphere. II. Effects of an influx of external oxygen. Icarus 145, 166–202.

Müller-Wodarg, I.C.F., Mendillo, M., Yelle, R.V., Aylward, A.D., 2004. A global circulation model of Saturn's thermosphere. Icarus. Submitted for publication.

Nicholson, P.D., French, R.G., Tollestrup, E., Cuzzi, J.N., Harrington, J., Matthews, K., Perković, O., Stover, R.J., 2000. Saturn's rings I: optical depth profiles from the 28 Sgr occultation. Icarus 145, 474–501.

Rishbeth, H., Garriott, O.K., 1969. Introduction to Ionospheric Physics. Academic Press, London.

Samson, J.A.R., 1966. The measurements of the photoionization cross-sections of the atomic gases. Adv. At. Mol. Phys. 2, 177–261.

Sandel, B.R., Shemansky, D.E., Broadfoot, A.L., Holberg, J.B., Smith, G.R., McConnell, J.C., Strobel, D.F., Atreya, S.K., Donahue, T.M., Pomphery, R.B., 1982. Extreme ultraviolet observations from the Voy-ager 2 encounter with Saturn. Science 215, 548–553.

Schunk, R.W., Nagy, A.F., 2000. Ionospheres: Physics, Plasma Physics, and Chemistry. Cambridge Univ. Press, New York.

Shimizu, M., 1980. Strong interaction between the ring system and the ionosphere of Saturn. Moon Planets 22, 521–522.

Tobiska, W.K., Woods, T., Eparvier, F., Viereck, R., Floyd, L., Bouwer, D., Rottman, G., White, O.R., 2000. The SOLAR2000 empirical solar irradiance model and forecast tool. J. Atm. Solar Terr. Phys. 62, 1233–1250.

Waite Jr., J.H., 1981. The ionosphere of Saturn. Thesis. Univ. of Mich., Ann Arbor.

Waite Jr, J.H., Cravens, T.E., 1987. Current review of the Jupiter, Saturn, and Uranus ionospheres. Adv. Space Res. 7 (12), 119–134.

Weiser, H., Vitz, R.C., Moos, H.W., 1977. Detection of Lyman α emission from the saturnian disk and from the ring system. Science 197, 755–757.

Yan, M., Sadeghpour, H.R., Dalgarno, A., 1998. Photoionization cross-sections of He and H_2. Astrophys. J. 496, 1044–1050.

Yelle, R.V., Miller, S., 2004. Jupiter's thermosphere and ionosphere. In: Bagenal, F., McKinnon, W., Dowling, T. (Eds.). Jupiter: Planet, Satel-lites and Magnetosphere. Cambridge Univ. Press, Cambridge. In press.

Yelle, R.V., 1988. H_2 emissions from the outer planets. Geophys. Res. Lett. 15, 1145–1148.